
This is an electronic reprint of the original article.
This reprint may differ from the original in pagination and typographic detail.

Myllys, M.; Kilpua, E. K J; Lavraud, B.; Pulkkinen, T. I.

Solar wind-magnetosphere coupling efficiency during ejecta and sheath-driven geomagnetic storms

Published in:
Journal of Geophysical Research: Space Physics

DOI:
[10.1002/2016JA022407](https://doi.org/10.1002/2016JA022407)

Published: 01/01/2016

Document Version
Publisher's PDF, also known as Version of record

Please cite the original version:
Myllys, M., Kilpua, E. K. J., Lavraud, B., & Pulkkinen, T. I. (2016). Solar wind-magnetosphere coupling efficiency during ejecta and sheath-driven geomagnetic storms. *Journal of Geophysical Research: Space Physics*, 121(5), 4378–4396. <https://doi.org/10.1002/2016JA022407>

This material is protected by copyright and other intellectual property rights, and duplication or sale of all or part of any of the repository collections is not permitted, except that material may be duplicated by you for your research use or educational purposes in electronic or print form. You must obtain permission for any other use. Electronic or print copies may not be offered, whether for sale or otherwise to anyone who is not an authorised user.

RESEARCH ARTICLE

10.1002/2016JA022407

Special Section:

Unsolved Problems in
Magnetospheric Physics

Key Points:

- The PCN index shows a clear solar wind Alfvén Mach number dependence, while AE and SYM-H do not
- Statistically, PCN index saturates during low and high Alfvén Mach number conditions
- PCN and AE indices saturate, but SYM-H does not

Supporting Information:

- Supporting Information S1

Correspondence to:

M. Myllys,
minna.myllys@helsinki.fi

Citation:

Myllys, M., E. K. J. Kilpua, B. Lavraud, and T. I. Pulkkinen (2016), Solar wind-magnetosphere coupling efficiency during ejecta and sheath-driven geomagnetic storms, *J. Geophys. Res. Space Physics*, 121, 4378–4396, doi:10.1002/2016JA022407.

Received 19 JAN 2016

Accepted 14 APR 2016

Accepted article online 2 MAY 2016

Published online 21 MAY 2016

Solar wind-magnetosphere coupling efficiency during ejecta and sheath-driven geomagnetic storms

M. Myllys¹, E. K. J. Kilpua¹, B. Lavraud^{2,3}, and T. I. Pulkkinen⁴

¹Department of Physics, University of Helsinki, Helsinki, Finland, ²Institut de Recherche en Astrophysique et Planétologie, Toulouse, France, ³Centre National de la Recherche Scientifique, Toulouse, France, ⁴Aalto University School of Electrical Engineering, Aalto, Finland

Abstract We have investigated the effect of key solar wind driving parameters on solar wind-magnetosphere coupling efficiency during sheath and magnetic cloud-driven storms. The particular focus of the study was on the coupling efficiency dependence with Alfvén Mach number (M_A). The efficiency has been estimated using the dawn-dusk component of the interplanetary electric field (E_y), Newell and Borovsky functions as a proxy for the energy inflow and the polar cap potential (PCN), and auroral electrojet (AE) and SYM-H indices as the measure of the energy output. We have also performed a time delay analysis between the input parameters and the geomagnetic indices. The optimal time lag and smoothing window length depend on the coupling function used and on the solar wind driver. For example, turbulent sheaths are more sensitive to the time shift and the averaging interval than smoother magnetic clouds. The results presented in this study show that the solar wind-magnetosphere coupling efficiency depends strongly on the definition used, and it increases with increasing M_A . We demonstrate that the PCN index distinctively shows both a Mach number dependent saturation and a Mach number independent saturation, pointing to the existence of at least two underlying physical mechanisms for the saturation of the index. By contrast, we show that the AE index saturates but that the saturation of this index is independent of the solar wind Mach number. Finally, we find that the SYM-H index does not seem to saturate and that the absence of saturation is independent of the Mach number regime. We highlight the difference between the typical M_A conditions during sheath regions and magnetic clouds. The lowest M_A values are related to the magnetic clouds. As a consequence, sheaths typically have higher solar wind-magnetosphere coupling efficiencies than magnetic clouds.

1. Introduction

As the solar wind reaches Earth, it interacts with its magnetosphere and disturbs its near space environment. The strongest geomagnetic disturbances are typically driven by interplanetary coronal mass ejections (ICMEs). An ICME consists of two main geoeffective structures with distinct solar wind plasma and magnetic field properties [Guo *et al.*, 2010; Kilpua *et al.*, 2013a]: first, an ejecta with typically smooth solar wind driving parameters preceded by a turbulent sheath region. The subset of ejecta can be described as magnetic flux ropes, i.e., magnetic clouds [Burlaga, 1988], which have a smoothly rotating magnetic field direction over an interval of about a day, combined with low plasma beta. Second, sheath regions are typically characterized by large amplitude magnetic field variations and compressed solar wind plasma.

Several studies have demonstrated that different solar wind conditions, for example, the sheath and the ejecta, lead to differences in the solar wind-magnetosphere coupling and magnetospheric activity [Huttunen *et al.*, 2002, 2004, 2006; Pulkkinen *et al.*, 2007; Nikolaeva *et al.*, 2011; Guo *et al.*, 2011; Yermolaev *et al.*, 2012; Lu *et al.*, 2013; Jing *et al.*, 2014]. Huttunen and Koskinen [2004] showed by analyzing the behavior of various geomagnetic indices that sheath regions typically lead to strong enhancements of high-latitude ionospheric currents (AE, AL, and also Kp), while magnetic clouds are more effective in enhancing the equatorial ring current (Dst and SYM-H). Yermolaev *et al.* [2012] demonstrated that sheath regions have a higher coupling efficiency than magnetic clouds. The authors determined the coupling efficiency of different interplanetary drivers using the ratio of magnetospheric indices (Dst, AE, and Kp) to the integrated interplanetary magnetic field (IMF) Z component (B_z) and solar wind driving electric field E_y . In turn, Guo *et al.* [2011] found similar

energy partitioning and efficiencies for sheath and ICME-driven intense ($Dst < -100$ nT) storms, while the means of the input energy and auroral precipitation were significantly different. The study used the methods outlined in *Turner et al.* [2009] to estimate the total energy dissipation in the ring current and in the ionosphere through Joule heating and precipitation. To estimate the coupling efficiency between the solar wind and the magnetosphere, *Guo et al.* [2011] [see also *Guo et al.*, 2010 and *Pulkkinen et al.*, 2015] used the Newell formula [*Newell et al.*, 2007] and the Borovsky function [*Borovsky*, 2008].

The reasons behind different magnetospheric responses to the sheaths and magnetic clouds are currently not well understood. Sheath regions have significantly higher level of turbulence which may enhance the transfer of solar wind plasma and energy into the magnetosphere through increased viscous interaction and instabilities at the magnetopause, e.g., Kelvin-Helmholtz vortices [*Borovsky and Funsten*, 2003; *Kilpua et al.*, 2013b; *Kavosi and Raeder*, 2015]. It is also shown by *Jing et al.* [2014] that the traditional coupling functions which use the upstream solar wind measurements, like Akasofu's epsilon parameter [*Akasofu*, 1981], do not include any hysteresis effects. *Jing et al.* [2014] studied the sudden turnings of IMF orientation on 5 June 1998 using the MHD simulations and showed that the epsilon parameter and mechanical and electromagnetic energy fluxes change slowly and consistently with the relatively stable B_z and density solar wind. However, during and after dramatic changes in density and B_z direction, the response of epsilon parameter and energy fluxes is slightly different. The sheath regions are more fluctuating than magnetic clouds, and typically consists of rapid changes in IMF magnitude and orientation. Thus, the absence of the hysteresis effects can cause differences for the observed solar wind-magnetosphere coupling between these structures when the efficiency is defined using the traditional coupling functions.

In other recent studies the importance of the solar wind Alfvénic Mach number (M_A , ratio of the flow velocity to the Alfvén speed) for solar wind-magnetosphere coupling has been highlighted [*Lavraud and Borovsky*, 2008; *Lopez et al.*, 2010].

Before reaching the magnetopause the solar wind is transmitted through the bow shock. As the plasma is super Alfvénic and supersonic, the properties of plasma and magnetic field changes across the shock depend on the value of the upstream M_A [e.g., *Lavraud et al.*, 2007, 2013]. The M_A is thought to influence the saturation of the electric potential across the polar cap. The cross polar cap potential (CPCP) is the difference between the maximum and the minimum of the potential in one hemisphere, and it can be considered as a measure of the magnetospheric convection state. It is known that during intense solar wind driving, CPCP saturates [*Reiff et al.*, 1981; *Reiff and Luhmann*, 1986; *Weimer et al.*, 1990; *Russell et al.*, 2001; *Raeder and Lu*, 2005; *Hairston et al.*, 2005; *Wilder et al.*, 2011]. This means that the response of the CPCP to solar wind electric field (E_y) driving becomes less efficient with increasing E_y .

When M_A is low, CPCP can saturate also during moderate E_y [*Lavraud and Borovsky*, 2008; *Lopez et al.*, 2010]. Low M_A periods are typically observed during magnetic clouds [*Lavraud and Borovsky*, 2008; *Guo et al.*, 2011], while in the sheath regions M_A is typically higher and more variable. *Guo et al.* [2011] noted, using a superposed epoch analysis, that the peak value of the Borovsky coupling parameter is larger for sheath-driven storms than for CME-driven storms, while no such a difference was observed for the Newell parameter. The high Borovsky parameter value was related to times when the sheath regions had higher M_A values than the ICMEs.

In this study we investigate the effect of key solar wind driving parameters on the solar wind-magnetosphere coupling efficiency and saturation of the polar cap potential during sheath and magnetic cloud-driven storms. The above-discussed studies emphasized the importance of M_A in controlling the coupling efficiency and CPCP saturation, and therefore, a particular focus is on the dependence with M_A . We examine here the instantaneous driving efficiency using several coupling functions.

The first part of the paper studies the time dependence between the geomagnetic indices and the interplanetary electric field Y component (E_y , GSM coordinate system), Newell and Borovsky functions. Since we are studying the instantaneous coupling efficiency instead of average efficiencies over solar wind structure, we need to take into account the time lag between the solar wind and the magnetosphere. The time delay analysis is presented in section 3 to motivate the methods which are used later in the study of the coupling efficiency. Section 4 presents the actual results, and sections 5 and 6 conclude the paper with discussion and summary.

2. Data and Methods

2.1. Data

We have used satellite measurements of the IMF and electric field components in GSM coordinates, the solar wind speed (v_{sw}), the dynamic pressure (P_{dyn}), the solar wind proton density (n), temperature (T), magnetosonic (M_{MS}), and Alfvén (M_A) Mach numbers. These data are obtained through the Near-Earth Heliospheric Data Base (OMNI, <http://omniweb.gsfc.nasa.gov/>) with 1 min resolution. OMNI data is composed of the solar wind measurements from several spacecraft in geocentric or Lagrangian point L1 orbits (at the time of this study the data consists mainly of Wind and ACE measurements). The data are propagated to the assumed bow shock location. The geomagnetic index data (PCN , AE , and $SYM-H$) are also downloaded from OMNIWeb with 1 min resolution.

2.2. Event Selection and Distributions of Solar Wind Parameters During Sheath Regions and Magnetic Clouds

The sheath and magnetic cloud intervals analyzed in this work are selected using the ACE interplanetary coronal mass ejection (CME) catalog maintained at the ACE Science Center. The catalog gives the shock time and the start and end times of the magnetic cloud. The typical sheath and magnetic cloud solar wind signatures are discussed, e.g., in *Zurbuchen and Richardson* [2006] and *Kilpua et al.* [2013b]. We selected in this study the events where either a sheath or magnetic cloud (or both) drove at least a moderate magnetic storm ($SYM-H < -50$ nT). In addition, the included events have a clear transition from the sheath to the magnetic cloud. To increase sheath-related data points, we also included events where a clear sheath region was observed, but no clear magnetic cloud followed, e.g., the CME was intercepted from the flanks and may rather be called ejecta in such cases.

Figure 1 shows the distributions of several solar wind parameters during the studied magnetic clouds (blue curves) and sheath regions (red curves). The sheath regions are shorter in duration than the magnetic clouds (in our data set the average durations were 11.44 h and 25.43 h for sheaths and magnetic clouds, respectively), and thus, the sheaths have fewer data points.

While the solar wind speed and IMF magnitude distributions are rather similar between sheaths and magnetic clouds, the solar wind density and temperatures tend to be much higher in sheath regions (Figure 1). As a consequence, sheaths have typically higher P_{dyn} , M_A , and V_A , and higher plasma beta than magnetic clouds. Low Alfvén Mach numbers ($M_A < 5$) are observed predominantly during magnetic clouds.

2.3. Coupling Efficiency and Coupling Functions

The coupling efficiency (eff) is defined as the ratio of the output to input into the magnetosphere-ionosphere system

$$\text{eff} = \frac{\text{output}}{\text{input}} \quad (1)$$

We use three solar wind-magnetosphere coupling functions to estimate the energy input: E_γ , Newell [Newell et al., 2007] and Borovsky functions [Borovsky, 2008]. The Newell function is

$$\frac{d\Phi}{dt} = v_{sw}^{4/3} B_T^{2/3} \sin^{8/3} \left(\frac{\theta}{2} \right) \quad (2)$$

where B_T and θ are the magnetic field perpendicular to the Sun-Earth line and the IMF clock angle. The Newell function has been constructed by “tuning” the best coupling functions in the literature. It describes the amount of the magnetic flux opening by magnetic reconnection at the magnetopause.

The Borovsky function has been derived using a different approach. It is based on the assumption that reconnection is a local process. The function is derived based on the Cassak-Shay formula [Cassak and Shay, 2007], and it states that dayside reconnection depends on the magnetic field strength and the mass density in the magnetosheath and in the magnetosphere. The Cassak-Shay formula was parametrized using global MHD simulations and the Earth’s magnetosheath properties. The physical interpretation of the function is that whatever controls these four free parameters in the Cassak-Shay formula controls the reconnection rate, and according to the Borovsky function, these parameters are mostly controlled by the solar wind pressure and M_A . The definition of the Borovsky function is

$$R = 0.4 \mu_0^{1/2} \sin \left(\frac{\theta}{2} \right) \rho v^2 (1 + 0.5 M_{MS}^{-2}) (1 + \beta_s)^{-1/2} \cdot [C\rho + (1 + \beta_s)^{-1/2} \rho_m]^{-1/2} [(1 + \beta_s)^{1/2} + 1]^{-1/2} \quad (3)$$

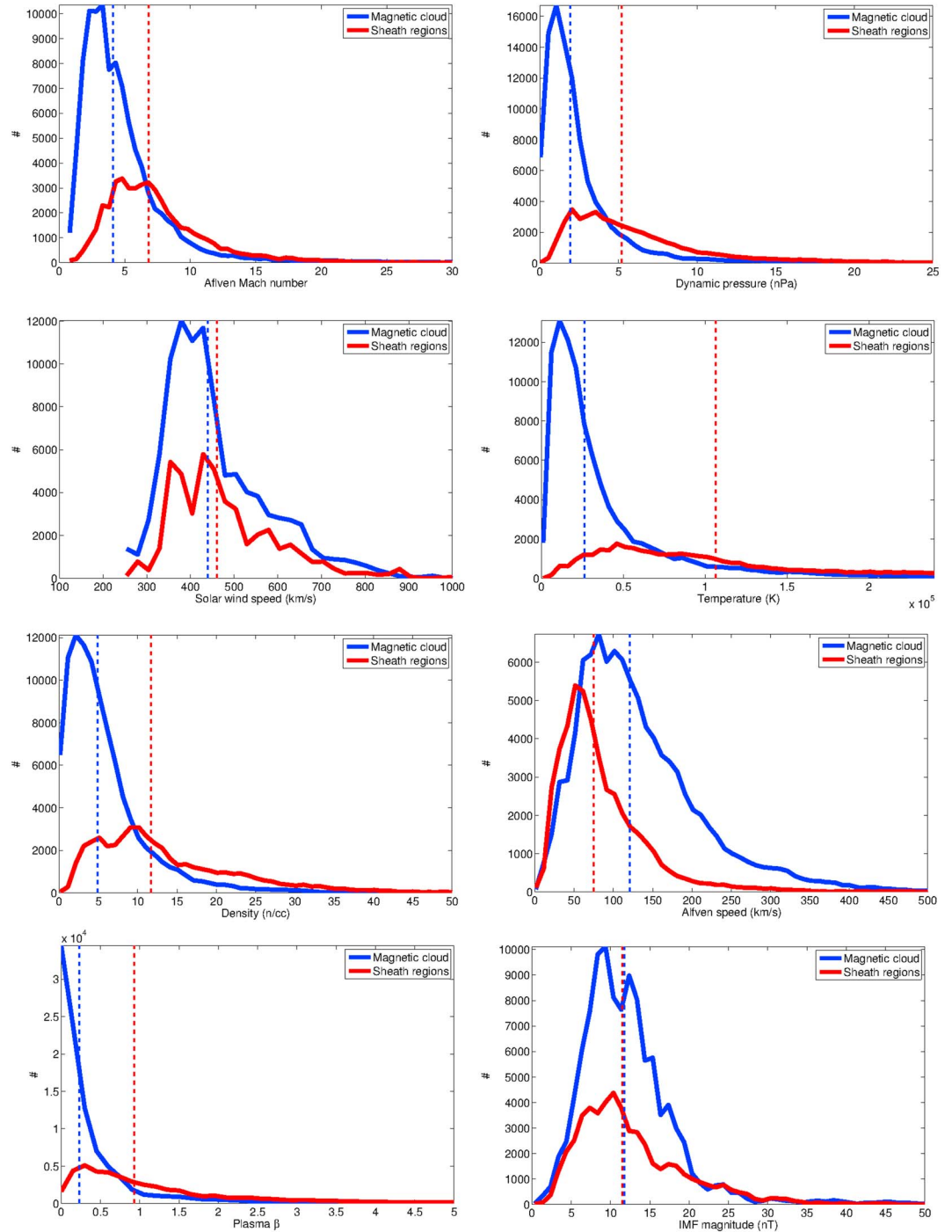


Figure 1. Distributions of the solar wind parameters during the studied magnetic cloud and sheath regions. The vertical dashed lines represents the median values of the distributions.

where β_s is the plasma beta of the magnetosheath,

$$\beta_s = 3.2 \cdot 10^{-2} M_A^{1.92} \quad (4)$$

and C is the compression ratio of the bow shock

$$C = \left[\left[1/4 \right]^6 + \left[1 / (1 + 1.38 \log_e(M_A)) \right]^6 \right]^{-1/6} \quad (5)$$

ρ_m is the magnetospheric mass density, which is set to zero since there is no information available about this value for the present statistical analysis. The same was done by Borovsky [2008]. The physical interpretation of

Table 1. Summary of the Time Lags Defined by Previous Studies

Author	Magnetospheric Index	Solar Wind Parameters	Time Lags
<i>Meng et al.</i> [1979]	Midday auroral oval motion	B_Z variations	17 min
<i>Bargatze et al.</i> [1985]	AL	VB_S	20 min and 60 min
<i>Ridley et al.</i> [1998]	The ionospheric convection pattern	IMF change (B_Z and B_Y)	8.4 (\pm 8.2) min
<i>Eriksson et al.</i> [2000]	Φ_{PC}	IMF B_Z , ϵ	15 min, 55 min, and 105 min
<i>Eriksson et al.</i> [2000]	ASY-H	IMF B_Z and ϵ	75 min
<i>Eriksson et al.</i> [2000]	Dst and SYM-H	IMF B_Z , ϵ	70 min
<i>Stauning et al.</i> [2008]	PC	E_M at 12 R_E	20 min

the term including ρ_m is to take into account the plasmasphere effect, which may reduce the reconnection rate on the dayside magnetopause. Thus, by setting ρ_m to zero we make the assumption that the plasmaspheric plume does not affect the reconnection rate in a major way. However, even if the plasma plumes may be infrequent enough to impact the results of this study, in general, this assumption should be treated with caution. There are statistical evidence that the reconnection jet velocity is lowered by the plasma plumes which may be a sign of lower reconnection efficiency [Walsh et al., 2013].

Both the Newell and the Borovsky functions show a good correlation with geomagnetic activity [Newell et al., 2007; Borovsky, 2008]. The differences between the functional form of the formulas are that the Borovsky function explicitly takes into account the Mach number and solar wind pressure dependence of the dayside reconnection rate. The study by Guo et al. [2010] showed that the average behavior of the Borovsky and Newell functions during magnetic clouds and their sheath regions are similar except during the high M_A and dynamic pressure conditions.

2.4. Geomagnetic Indices

The energy output is estimated using the geomagnetic indices PCN, AE, and SYM-H. Similar definitions of the coupling efficiency have been used earlier, e.g., by Palmroth et al. [2007] and Yermolaev et al. [2012]. The geomagnetic indices measure different magnetospheric phenomena and current systems (i.e., different energy sinks). The AE index represents the overall activity of the auroral electrojets. The AE index is derived from geomagnetic variations in the horizontal component observed at nine high-latitude magnetometer observatories along the auroral zone in the northern hemisphere [Rostoker, 1972]. The PCN index represents polar cap magnetic variation relation to magnetospheric convection above the polar cap. It is derived from ground based geomagnetic measurements within the northern polar cap [Troshichev et al., 1988]. Observations from only one station (Thule) are used. SYM-H is a 1 min index describing the ring current activity. The SYM-H is derived using six magnetometer stations near the equator [Iyemori and Rao, 1996].

3. Time Delay and Time Window Analysis

As a first step, we investigate the optimal time delay, as well as averaging window length used to smooth the solar wind parameters for studying the coupling functions. We combine instantaneous, 1 min values of geomagnetic indices with the solar wind energy input using the three coupling functions described in section 2.2.

3.1. Summary of Past Studies

There are several past studies investigating the time lag between geomagnetic indices and solar wind parameters/coupling functions, summarized in Table 1. For instance, Ridley et al. [1998] studied the changes in ionospheric convection associated with changes in the IMF Y and Z components at the magnetopause. The obtained communication time between the IMF and the onset of reconfiguring of the ionospheric convection pattern was 8.4 (\pm 8.2) min. Eriksson et al. [2000] found 70–75 min time lags between the 5 min averaged IMF Z component and epsilon parameter and geomagnetic indices Dst, SYM-H, and ASY-H. The cross polar cap potential (Φ_{PC}) showed several time lags: 15, 55, and 105 min. The Φ_{PC} was estimated based on the 37 polar cap crossings of the FAST and Wind satellite measurements. In turn, Stauning and Troshichev [2008] found a 20 min time delay between the geoeffective electric field E_M ($E_M = v_{SW} B_T \sin^2 \left(\frac{\theta}{2} \right)$) at 12 R_E and PCN, but the first response from the dynamic pressure pulse was seen in only 5 min.

Furthermore, the magnetospheric-ionospheric system is suggested to be insensitive to fast variations of the solar wind input parameters, and to act like a low-pass filter [Clauer *et al.*, 1981; Takalo *et al.*, 2000; Ilie *et al.*, 2010]. Takalo *et al.* [2000] concluded in their study that the high-frequency part of AE is produced by intrinsic dynamics of the magnetosphere, while the low frequencies are well correlated with $v_{sw}B_S$, where B_S is defined by

$$B_S = 0, B_Z \geq 0 \quad B_S = -B_Z, B_Z < 0 \quad (6)$$

In addition, simulations have shown that small timescale fluctuations do not affect CPCP. Ilie *et al.* [2010] used the Space Weather Modeling Framework (SWMF) [Toth *et al.*, 2005] to analyze CPCP response to different solar wind parameters for four sliding average window lengths (4, 60, 120, and 180 min). The results showed that CPCP had very similar behavior in all cases, which indicates that small timescale fluctuations do not affect the cross polar cap potential in the simulations.

3.2. Our Approach

Contrary to previous studies which only searched for the time lag (τ), we also investigate the optimal time window, which is used to average the solar wind parameters. Both the time lag and the window length are expected to depend on the coupling function and on the geomagnetic index used (as they partly reflect different regions where energy is dissipated and different energy transfer mechanisms). The following procedure has been used to obtain the most optimal τ and time window pair:

1. The correlation coefficient is computed between the coupling function and the geomagnetic index when time window is kept fixed and the time lag is varied.
2. Computed correlation coefficients are stored into matrix elements.
3. The time window value is changed.
4. The correlation coefficients with the new time window value are computed again by varying the time lag.

The following steps are repeated until the wanted maximum time window length is achieved. As a results, we get a matrix which rows represents different time window and the columns time lag values.

For the PCN and AE indices the time lag is varied from 1 to 60 min and for the SYM-H from 1 to 120 min. Time window is centered on τ , and thus, the maximum window length can be only twice the τ value. This means that the maximum time window for PCN and AE is 120 min and for the SYM-H 240 min.

We calculate correlation coefficients using two approaches: Spearman's rank correlation and Pearson product-moment correlation coefficient. The Spearman's rank correlation uses a nonparametric dependence between two parameters, and it measures the monotonic relationship of the parameters. The Pearson correlation is a measure of the linear dependence between normally distributed parameters. Earlier studies have shown that the dependence between E_V and the PCN index is mostly linear, but the saturation of the polar cap causes nonlinearity to the relationship, as discussed in section 1. Since we want to avoid preconception on the linear dependence between the solar wind parameters and the geomagnetic indices, we did the correlation analysis study using both of these definitions.

It is also worth mentioning that in previous publications [Bargatze *et al.*, 1985; Stauning and Troshichev, 2008], correlation studies between E_V and geomagnetic indices have been done using only positive E_V values. We compute the correlation using all E_V values.

The most optimal values for τ and window length obtained using our method are listed in Table 2. The table shows the results for all three coupling functions and geomagnetic index combinations for sheath and magnetic clouds separately and for these structures combined using both the Spearman and Pearson correlation coefficients. For sheath regions we added two extra hours before the shock to observe the effect of the time shift more clearly.

3.3. Correlation Coefficient Analysis for Magnetic Cloud Events

The color maps based on Spearman's rank correlation coefficient for magnetic clouds are shown in Figure 2. The horizontal axis represents the time lag and the vertical axis the averaging time window. The color of the bin shows the value of the correlation coefficient with related color bar plotted on the right of each plot. Equivalent maps were also created using the Pearson's correlation coefficients (not shown). For the PCN, these maps were found to be similar as the Spearman's maps, while for AE and SYM-H there were some differences. We decided to use the Spearman correlation coefficient because it does not include any assumption on how the parameters are distributed and it gives the highest correlations.

Table 2. The Result of the Time Lag and Window Study

Index	Method	SW Parameter	Sheath + Cloud		Sheath		Cloud	
			Lag	Window	Lag	Window	Lag	Window
PCN	Spearman	E_Y	49	97	49	97	31	61
PCN	Spearman	Newell	23	45	25	49	29	57
PCN	Spearman	Borovsky	18	31	17	27	20	39
PCN	Pearson	E_Y	60	119	54	119	41	81
PCN	Pearson	Newell	22	43	58	109	57	113
PCN	Pearson	Borovsky	17	33	15	29	60	119
AE	Spearman	E_Y	57	115	53	105	52	95
AE	Spearman	Newell	52	103	53	106	55	110
AE	Spearman	Borovsky	47	93	53	105	43	85
AE	Pearson	E_Y	60	119	46	91	60	119
AE	Pearson	Newell	46	91	32	64	60	119
AE	Pearson	Borovsky	26	51	18	35	60	119
SYM-H	Spearman	E_Y	120	239	119	239	120	87
SYM-H	Spearman	Newell	120	239	120	239	120	215
SYM-H	Spearman	Borovsky	120	215	120	109	120	35
SYM-H	Pearson	E_Y	120	239	120	239	120	119
SYM-H	Pearson	Newell	120	215	120	239	120	171
SYM-H	Pearson	Borovsky	120	215	120	239	120	165

For *AE* (Figure 2, middle column) and *SYM-H* (right column) the correlation coefficient maps have similar patterns for all three coupling functions. For *SYM-H* the correlation increases steadily with τ over the entire range up to 120 min. Hence, it is possible that the highest correlations are outside the studied time interval. The high τ value is expected because *SYM-H* is affected by the symmetrical part of the ring current [Iyemori and Rao, 1996] which builds up slowly [Gonzalez and Echer, 2005].

The correlations between the coupling functions and *AE* increases up to 20 min and after that the value seems to saturate. The saturation is probably related to the substorm cycle, which strongly controls the *AE* activity. The typical substorm cycle duration is between 2 and 4 h [Tanskanen et al., 2002].

The correlation increases for *PCN* (Figure 2, left column) with increasing time lag until the maximum value is reached around 20–30 min. After this local maximum, correlation starts to decline. This is true for all the input parameters. This indicates that *PCN* reacts quickly to the solar wind driving, but it has a short memory.

The color pattern of the correlation coefficient maps differs for each coupling function. For E_Y the regions of the highest correlation are found when τ and window are both high (window < 60 min and τ < 30 min). In the case of the Newell function the highest correlation coefficients can be found near $\tau = 20$ min for *PCN*, and the correlation increases with increasing window length. The area of high correlation is narrower and stands out more clearly for the Borovsky function. The Borovsky function also gives the smallest τ and the window lengths (Table 2) for *PCN* and *AE*, but on the other hand, the Newell function and E_Y give very similar results.

However, all maps show some similar features regardless of the coupling function and geomagnetic index. The correlation increases with increasing time window, and the region of high correlation is spread over a wide area. The trend that the correlation stays high and almost fixed when τ is kept constant and the window length is increased can be explained by the fact that when the window becomes larger than the smallest fluctuations in the solar wind, the effect of the averaging decreases and the correlation coefficient saturates. The correlation mostly comes from large fluctuations. Small fluctuations only add noise and lower the correlation.

We find that the correlation coefficient maps are very similar for the sheath and magnetic cloud combined (not shown) than for to ones including only magnetic clouds. This is due to the fact that magnetic clouds are often longer in duration than the sheath regions (see section 2.2). Hence, the combined maps are not shown here or discussed further.

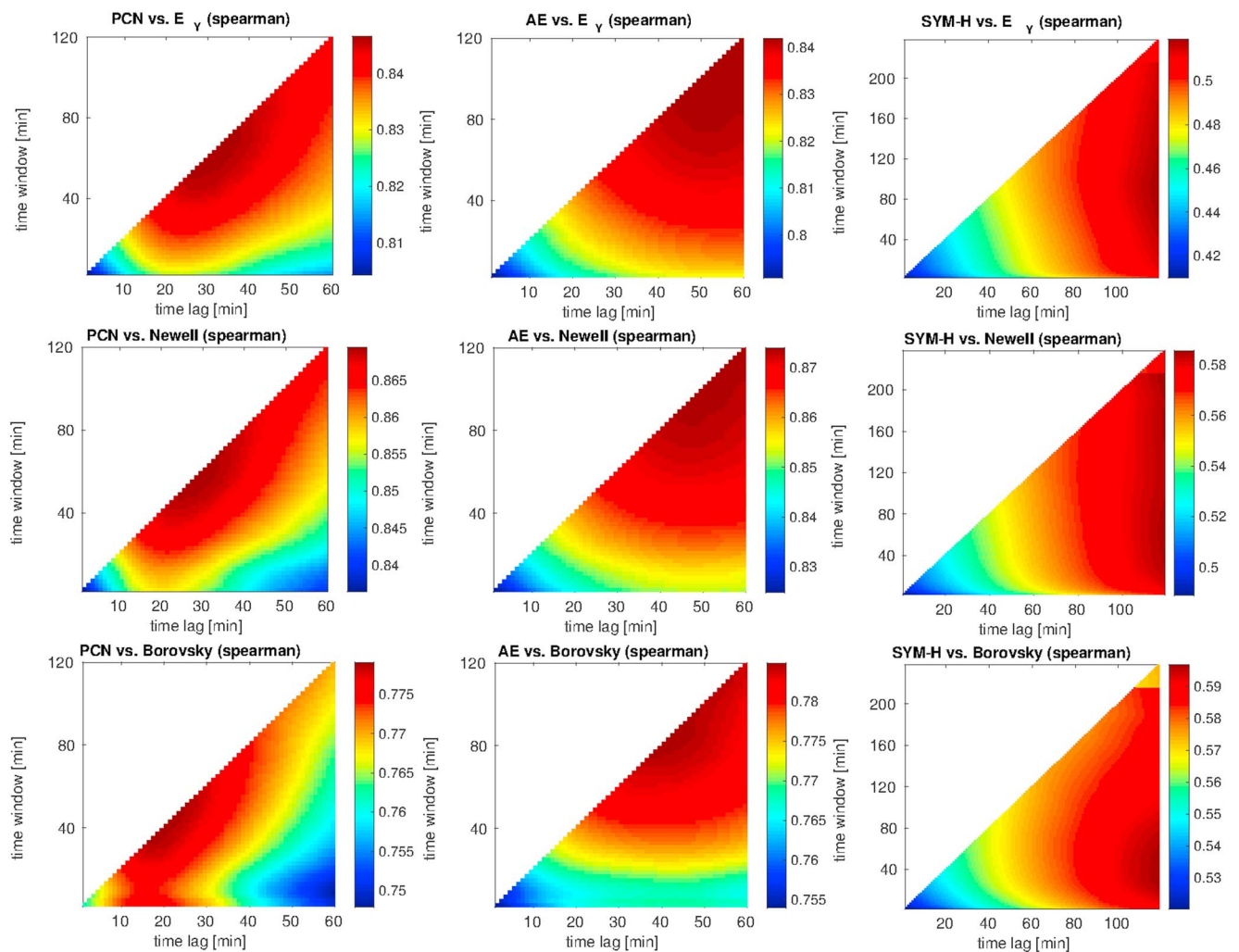


Figure 2. Correlation coefficients between geomagnetic indices (*PCN*, *AE*, and *SYM-H*) and input parameters (E_γ , Newell function and Borovsky function) during magnetic clouds. The horizontal axis shows the used time lag values and the vertical axis the averaging time window length.

3.4. Correlation Study During the Sheath Regions

The results for sheath regions are shown in Figure 3. There are some clear differences between the correlation coefficient maps for sheaths and magnetic clouds. (1) The highest correlations occur during the magnetic clouds, (2) the range of the correlation coefficient values are wider during the sheath regions, (3) the region of the highest correlation stands out more clearly during sheath regions, and (4) for magnetic clouds all the maps showing the correlation between the coupling functions and *PCN* have similar pattern. In the case of the sheath regions the *PCN* maps for E_γ is clearly different from the *PCN* maps for Newell and Borovsky functions.

The differences in the correlation coefficient maps highlight different solar wind conditions during magnetic clouds and their sheaths (see section 2.2). Because of the smoother variations of the solar wind input parameters during magnetic clouds, the time shift has a smaller effect on the correlation during magnetic clouds than during sheath regions. As a consequence, the correlation is not very sensitive to time delay for magnetic clouds. Because turbulent sheath regions have a more complicated structure, the correlation is more sensitive to the time shift. This explains why the correlation coefficients values have a broader distribution and the area of the highest correlations is more localized.

To further highlight the differences between magnetic clouds and their sheath regions, we show in Figure 4 time series of E_γ , Newell and Borovsky parameters as well as the *AE* and *PCN* indices during one of the event studied. This event occurred on 20 November 2003. It consists of a fluctuating sheath region between 20 November 2003 08:05 and 20 November 2003 11:45 UT and a smooth magnetic cloud between

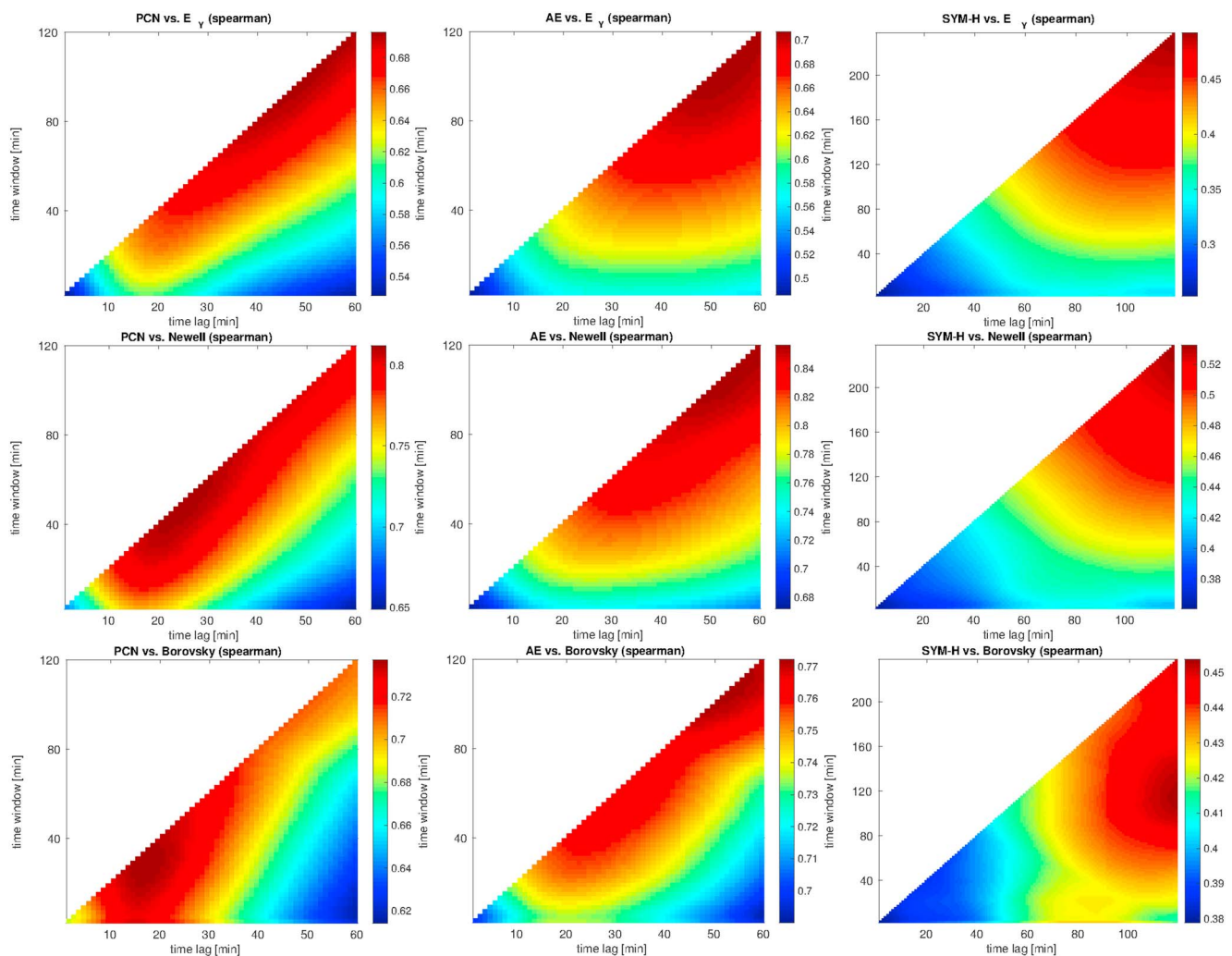


Figure 3. Correlation coefficients between geomagnetic indices (*PCN*, *AE*, and *SYM-H*) and input parameters (E_Y , Newell function and Borovsky function) during sheath regions. The horizontal axis shows the used time lag values and the vertical axis the averaging time window length.

20 November 2003 11:45 and 21 November 2003 07:28 UT, marked by vertical red lines. The correlation coefficient maps for the *PCN* (and *AE*) and E_Y for the magnetic cloud (Figure 4, top left) and sheath region (Figure 4, top right) are also shown. The maps show that the correlation is very high and almost constant during the cloud but the values vary a lot during the sheath region.

Based on the previously mentioned differences between the sheath regions and magnetic clouds, we conclude that the more structured sheath regions are more suitable for the time lag and window determination. Thus, we will use the time lag and window length values defined using the sheath region data and the Borovsky coupling function. The Borovsky function gives the lowest value for the time lag and window for *PCN* and *AE* indices and are close to values determined in past studies. The selected window and time lag values are listed in Table 3.

4. Results

4.1. Solar Wind Parameter Dependence of the *PCN*, *AE*, and *SYM-H* Indices

We investigate here how the responses of *PCN*, *AE*, and *SYM-H* as a function of solar wind driving electric field E_Y are organized by solar wind parameters. The solar wind parameters were averaged using the time window values given in Table 3. The used time lags between the solar wind input values and the indices can be found in the same table. The results are shown in Figure 5 (see also Figures S1 and S2 in the supporting information). All the studied data points (sheath + magnetic cloud combined) were divided into four groups based on the solar wind parameter distributions. The division into quartiles was done separately for each solar wind driving

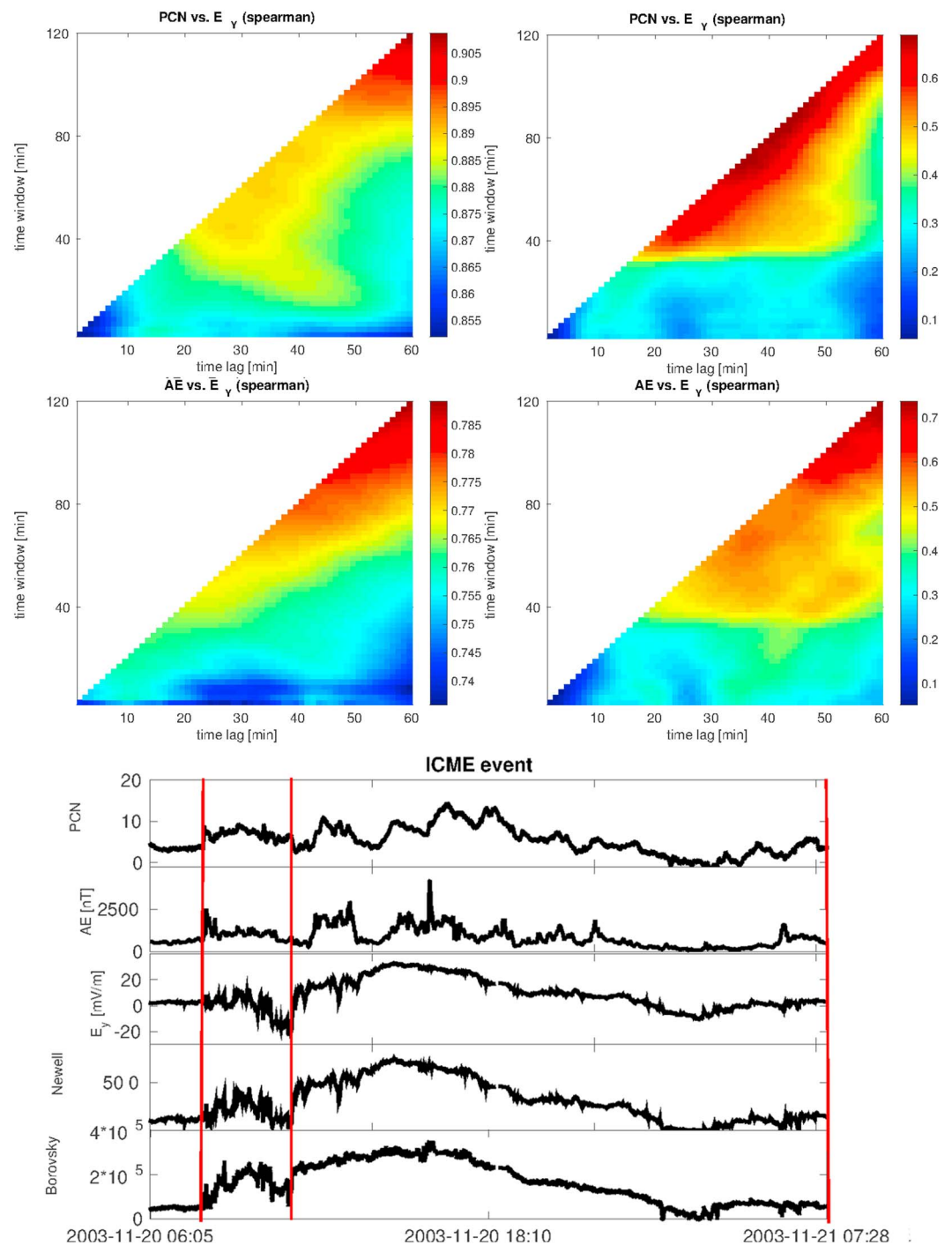


Figure 4. Case study example of the time delay analysis for the sheath and magnetic cloud event. The correlation coefficient during the (top left) magnetic cloud and (top right) during the sheath region. (bottom) The time series for the PCN and AE indices and E_y , Newell and Borovsky functions. The sheath region (20 November 2003 08:05–20 November 2003 11:45 UT) and magnetic cloud (20 November 2003 11:45–20 November 2003 07:28 UT) are marked using the red vertical lines.

Table 3. List of the Time Lag and Window Values Which are Used in This Study

Geomagnetic Index	Time Lag (min)	Time Window (min)
PCN	17	27
AE	53	105
SYM-H	120	109

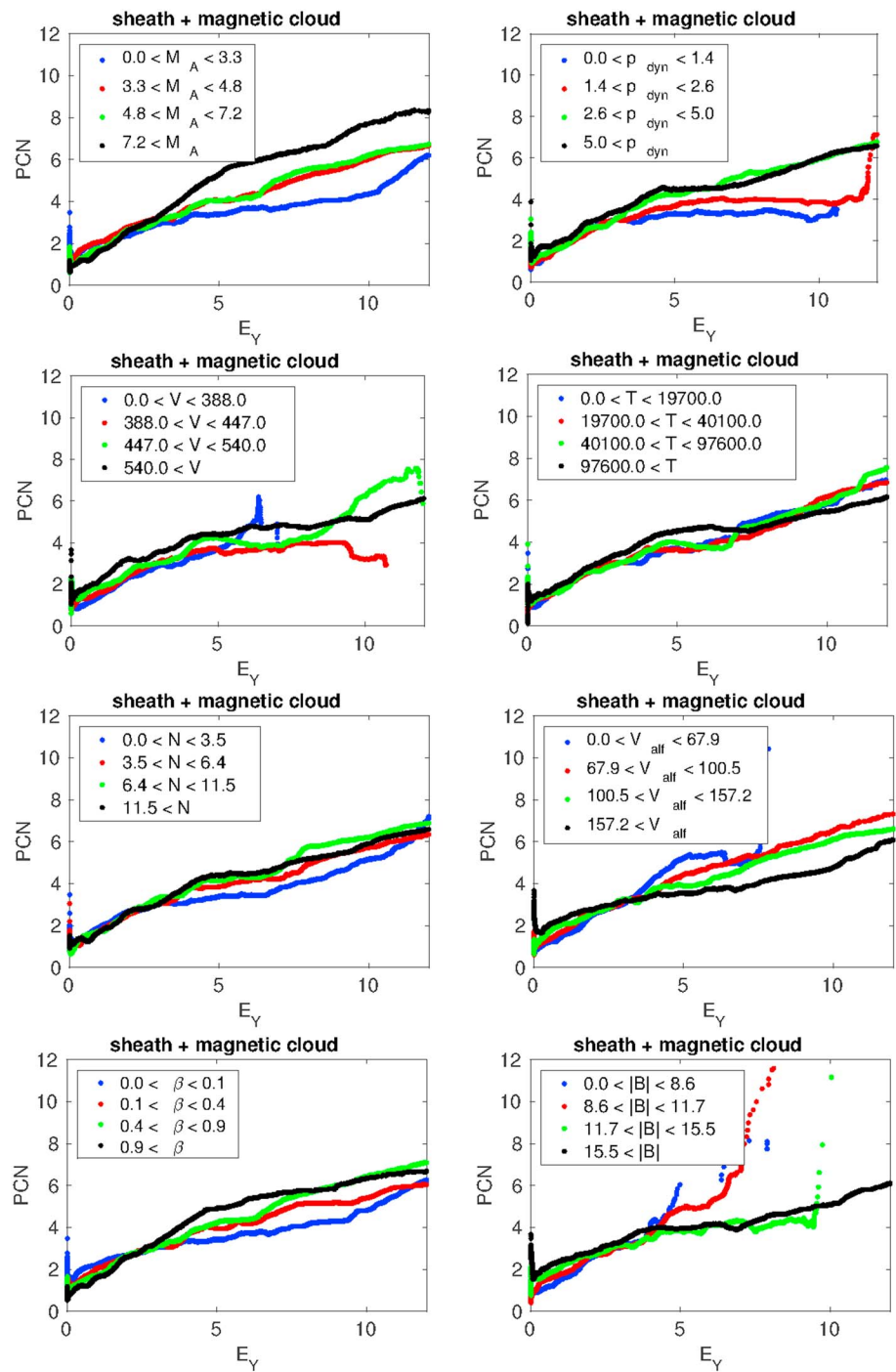


Figure 5. The PCN index as a function of E_Y during different (a) Alfvén Mach number, (b) dynamic pressure (nPa), (c) speed (km/s), (d) temperature (K), (e) density (n/cc), (f) Alfvén speed (m/s), (g) plasma beta, and (h) IMF magnitude (nT) levels during magnetic clouds and sheath regions.

Table 4. The Limit Values for the Solar Wind Parameter Quartiles

	M_A	V (km/s)	p_{dyn} (nPa)	T (K)	N (n/cc)	V_{alf} (km/s)	β	$ B $ (nT)
1	0–3.3	0–388	0–1.44	0–19,700	0–3.5	0–67.9	0–0.15	0–8.6
2	3.3–4.8	388–447	1.44–2.56	19,700–40,100	3.5–6.4	67.9–104.5	0.15–0.36	8.6–11.7
3	4.8–7.2	447–540	2.56–4.98	40,100–97,600	6.4–8.11.5	104.5–157.2	0.36–0.90	11.7–15.5
4	> 7.2	> 540	> 4.98	> 97,600	> 11.5	> 157.2	> 0.90	> 15.5

parameters (M_A , v_{SW} , P_{dyn} , etc.). The limits for each parameter are shown in Table 4. We have limited the study to time steps when E_Y is positive.

To show the underlying trend of the scattered data in each group, 2700-point running average is applied. The running average is plotted using different color for each group: the blue curve shows the lowest and the black curve the highest quartile of the parameters in question. Even if each group has around the same amount of data points, the points may be unevenly distributed as a function of E_Y . Thus, all curves do not cover the entire range of E_Y values. The data coverage for the highest E_Y is relatively low, which causes larger fluctuations in that regime.

Figure 5 (left column, first row) shows PCN as a function of E_Y for different M_A conditions. The figure shows a clear separation of the curves for $E_Y > 4$ mV/m. The most visible difference is between the blue (the lowest M_A) and the black (the highest M_A) curves. The blue curve exhibits saturation in the range $4 \text{ mV/m} < E_Y < 10 \text{ mV/m}$, while the other M_A curves increase more linearly. The interesting feature is that the black curve ($M_A > 7.2$) also saturates, but the saturation occurs for higher PCN values than for the low M_A curve. The fact that the saturation occurs for high M_A suggests that M_A is not necessarily the only factor causing the saturation. The investigation of the other panels in Figure 5 reveals that M_A is the parameter, among all studied solar wind parameters, which shows the most significant influence on polar cap saturation. For AE and SYM-H (see Figures S1 and S2 in the supporting information) we did not find any obvious dependence with any the investigated parameters, but discuss the relation to M_A further in the next section.

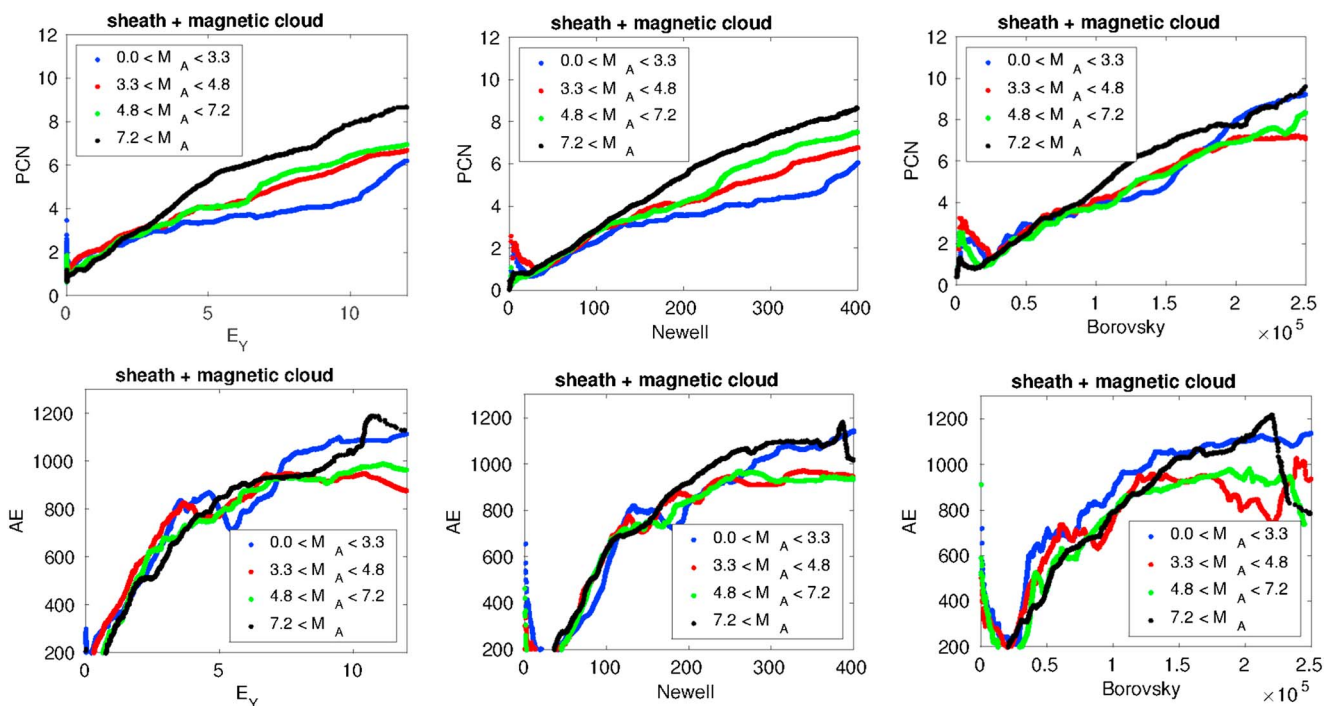


Figure 6. The geomagnetic indices (PCN and AE) as a function of E_Y , Newell and Borovsky functions during different Alfvén mach number levels.

Table 5. The E_y Limits for Different Driving Conditions

	E_y (mV/m)
Weak	1–2.5
Moderate	2.5–5
Intense	5–10
Strong	> 10

4.2. Coupling Functions Versus Geomagnetic Indices During Different M_A Conditions

In the previous section geomagnetic indices were displayed as a function of E_y during different solar wind conditions. PCN revealed a clear M_A dependence when $E_y > 4$ mV/m. To investigate how each coupling function accounts for the saturation, the top panels of Figure 6 show PCN as a function of E_y (left panel),

Newell function (middle panel) and Borovsky function (right panel). The colored curves represents again different M_A ranges, similar to Figure 5. The M_A dependence of PCN is clearly visible when the input energy is estimated using the E_y and Newell functions, but the dependence almost disappears when the Borovsky function is used. This comes from the fact that the Borovsky function explicitly includes M_A (see equation (5)). The PCN index as a function of the Newell function and E_y shows the influence of M_A and a clear saturation, i.e., the nonlinearity between the index and the coupling function. The AE index does not show much dependence on M_A and thus does not depend much on the coupling function used.

4.3. Coupling Efficiency as a Function of Alfvén Mach Number

In this section the coupling efficiencies are examined using equation (1). The input parameter is the solar wind driving electric field E_y . The output was estimated using PCN , AE , and $SYM-H$. All data points were divided into four different groups based on the intensity of E_y . The groups are called weak, moderate, intense and strong, and the limiting E_y values are listed in Table 5. The coupling efficiency in each group is plotted again as a function of M_A in Figure 7. The curves have been normalized based on the maximum value of the blue (weak driving) curve. Data points were smoothed using a moving average, with a window length which is 20% of the total number of data points in each group.

The following conclusions can be drawn from Figure 7: The efficiency decreases when the intensity of solar wind driving increases. The efficiency of PCN increases with increasing M_A . These results show that if PCN saturation is quantified by efficiency parameters, an M_A independent saturation process exists as a baseline and decreases the efficiency by over a factor of two (blue curve compared with the other curves). PCN saturation is however further enhanced through a M_A dependent effect, by a factor greater than 2, for all driving conditions, i.e., all curves decrease at low M_A . However unlike the PCN index, these results clearly show that the saturation of the AE index does not depend on M_A (all curves are essentially horizontal). The AE index also shows saturation, i.e., the efficiency decreases when E_y increases compared to weak (blue) driving. Finally, $SYM-H$ does not saturate much, if at all, compared to PCN and AE . All the curves for $SYM-H$ are very close to each other.

4.4. Error Analysis

Figures 5 and 7 show that saturation occurs even during high M_A conditions, which means that saturation is not primarily due to low M_A effect suggested before, for example, by *Lavraud and Borovsky [2008]* and *Lopez et al. [2010]*. In order to convincingly demonstrate that the saturation is not due to poor statistics in the nonlinear regime, we focus further analysis on the breakpoint (“knee,” see Figure 5) from linear to nonlinear behavior.

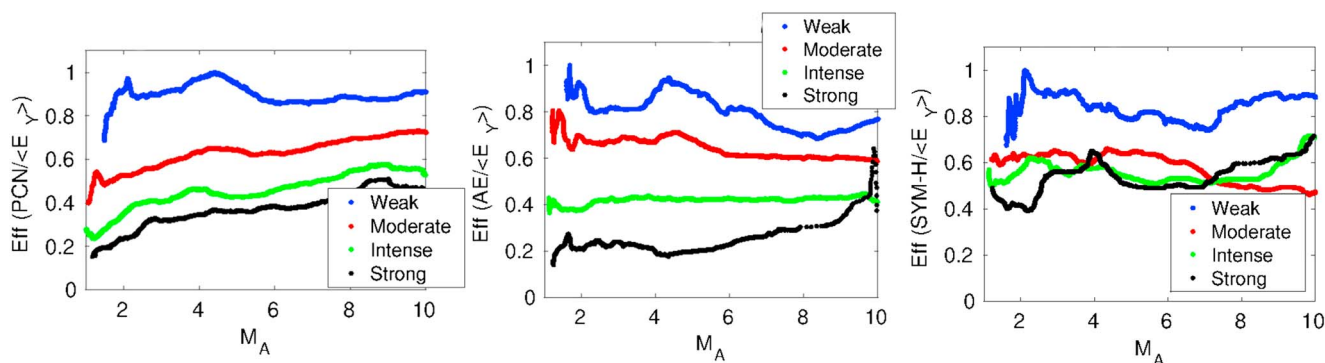


Figure 7. The coupling efficiency as a function of Alfvén Mach number for PCN , AE , and $SYM-H$ indices.

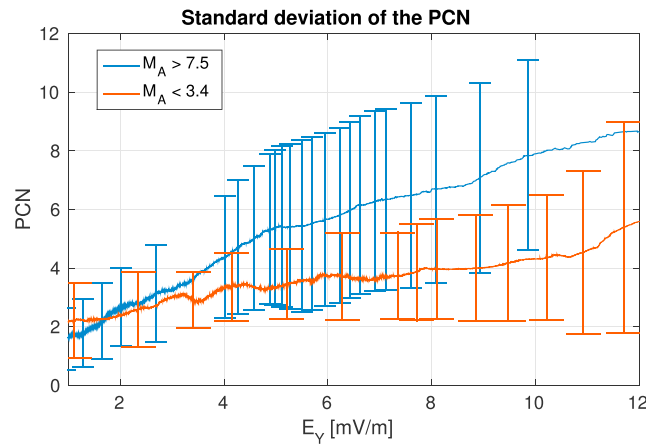


Figure 8. The smoothed PCN as a function of E_Y for the highest and lowest M_A periods. Error bars show the standard deviation of the PCN measurements.

points is significantly reduced the standard deviation starts to increase. The standard deviation for the red curve (low M_A) is also smaller than the distance between the two smoothed curves when E_Y is between 4 to 11 mV/m. Data points are more scattered (larger error bars) during high M_A conditions. The standard deviation increases as E_Y increases, but it does not show any sudden increase around the knee regime, i.e., near $E_Y \approx 5$ mV/m.

Figure 9 shows all data points with M_A above 7.2. The color of the data points represents the M_A value and the color panel on the left shows the scale. The black curve shows the 2700-point running average. We have also fitted a linear curve (red) to the data when $E_Y < 5$ mV/m. Because the smoothed (black) curve shows non-linearity between E_Y and PCN when E_Y exceeds 5 mV/m, the linear fit was done using the data points only from the linear part of the plot. Figure 9 reveals that the highest M_A values are nearly evenly distributed on both sides, above and below, of the linear prediction curve.

Figure 9 also shows very clearly that the linear prediction overestimates PCN when E_Y is above 5 mV/m. To illustrate this, we computed the distance of each data point from the linear regression. Distances are calculated in such a way that the measured value of PCN is subtracted from the linear prediction value ($PCN_{\text{predicted}} - PCN_{\text{measured}}$). Thus, a positive error means that the measured value is less than the predicted PCN and a negative error that the measured value exceeds the prediction. Distances are presented in histograms

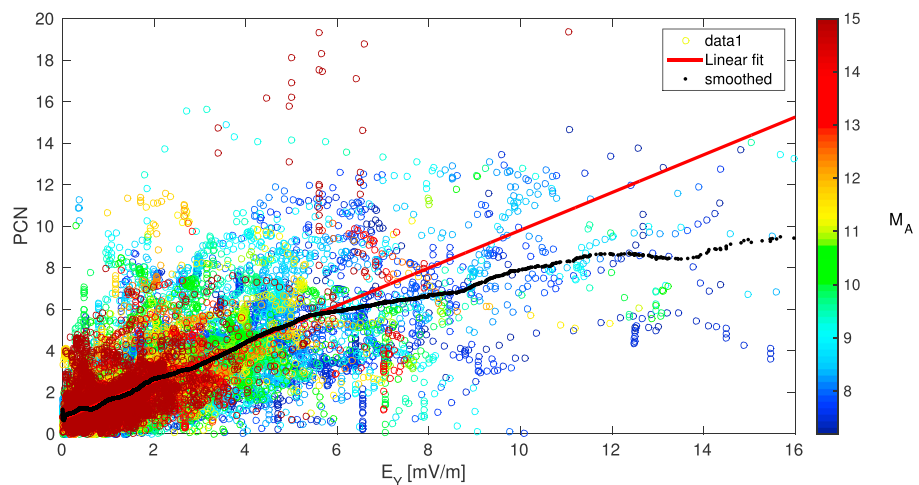


Figure 9. All the data points during $M_A > 7.2$ periods. The color of the data point represents the M_A value. The red curve is a linear regression which is fitted to the data points when $E_Y < 5$ mV/m. The black curve shows the smoothed PCN as a function of E_Y .

Figure 8 shows the smoothed curves for PCN as a function of E_Y for the highest ($M_A > 7.2$) and lowest ($M_A > 3.3$) M_A groups. The smoothing method is the same as explained in section 4.1. The error bars show the standard deviation of the PCN measurements within the window; thus, the bars describe the scatter of the points. The error bars are plotted more frequently near the knee point.

During low M_A conditions (red curve) the standard deviations are considerably smaller than during high M_A conditions (blue curve). The standard deviation for low M_A does not vary much when $E_Y < 8$ mV/m. When E_Y exceeds 8 mV/m and the number of data

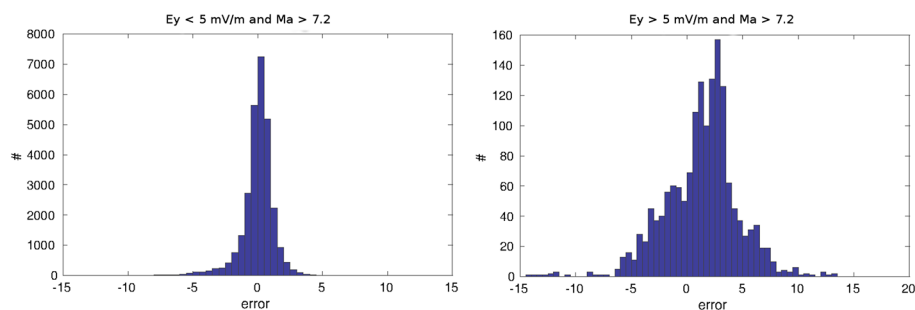


Figure 10. Histograms show the distance of the measurement points from the linear regression line ($\text{error} = PCN_{\text{predicted}} - PCN_{\text{measured}}$). The left histograms shows the error values when $E_Y < 5$ mV/m and the right when the $E_Y > 5$ mV/m.

in Figure 10. Figure 10 (left) shows a histogram for the errors when $E_Y < 5$ mV/m, and Figure 10 (right) when $E_Y > 5$ mV/m. There is a clear difference in the shape of the histograms. During the linear part of the $PCN-E_Y$ relation the errors are distributed almost symmetrically on both sides of zero. However, when E_Y is greater than 5 mV/m, histogram is biased on the side of positive errors, which is due to the fact that the linear prediction systematically overestimates the PCN value. Errors are also significantly higher during the nonlinear regime, because of the larger scatter of the data points.

As a summary, it is evident that the relationship between PCN and E_Y is more complicated during high M_A conditions than during low M_A conditions. Despite of the large scatter for high M_A conditions, it is clear that there is nonlinearity between PCN and E_Y when the solar wind driving exceeds 5 mV/m.

5. Discussion

The causes behind the CPCP saturation are still a controversial topic. Several models have been presented in the literature, which evoke different mechanisms to explain the observed CPCP saturation. Previous studies have shown that the saturation occurs over a wide range of E_Y values (see the introduction by *Ridley* [2005]). The smallest E_Y when the saturation has been observed is 3 mV/m [*Russell et al.*, 2000], but there are studies which have reported that the saturation occurs only at considerably higher E_Y values, e.g., with a threshold E_Y up to 15 mV/m [*Shepherd et al.*, 2002]. These differences in the limiting E_Y values may be explained by the fact that many solar wind parameters, like M_A , affect the saturation. In our study, during low M_A (< 3.3) conditions the saturation for PCN started to occur when E_Y exceed ~ 3 mV/m and in the high M_A regime (> 7.2) when the E_Y exceeded 5 mV/m. The AE saturation occurred above 6 mV/m independent of M_A .

The existing saturation models can be roughly divided into those where the saturation occurs due to decreasing dayside reconnection rate and those where the saturation is related to physical processes after the reconnection, i.e., coupling processes in the inner magnetosphere. We discuss below a few of these models, for a detailed description see, e.g., *Borovsky et al.* [2009].

The dayside magnetic reconnection at the magnetopause during positive E_Y conditions feeds the Region 1 current system via the MHD generator. The saturation model by *Hill et al.* [1976] suggests saturation of CPCP due to lowered reconnection rate at the dayside magnetopause during strong E_Y driving. According to the model, the reconnection is affected by the negative feedback from the enhanced Region 1 currents which close in the high-latitude ionosphere. The Region 1 currents create a magnetic field which opposes the Earth's dipole field at the dayside magnetopause. Hence, in the Hill model, the saturation would occur at times when the magnetic field induced by the enhanced Region 1 currents significantly weakens the magnetospheric side of the reconnecting magnetic field. Weakening of the magnetic field limits the reconnection rate by lowering the Alfvén speed at the reconnection site.

Raeder and Lu [2005] suggested that saturation is related to a shortened reconnection X line. The reduced X line length can decrease the total amount of reconnected flux between the solar wind and the magnetosphere and thus limits the CPCP. The authors studied CPCP saturation during the Bastille Day Storm and noted that the empirical model, which takes into account the X line length, gave the best predictions of the polar cap potential from the investigated models.

It is also expected that the CPCP saturation depends on the solar wind Alfvén Mach number. Alfvén wings form during the extreme case of sub-Alfvénic solar wind conditions, when the magnetic field bends around a conducting obstacle [Neubauer, 1980]. The bending launches Alfvén waves, which propagate with the Alfvén speed (v_A) along the magnetic field lines. The plasma flow still affects the magnetic field lines and the Alfvén waves travel with angle $\theta = (M_A^{-1})$. The interaction with the flow velocity and the Alfvén wave creates a cavity which the flow characteristics are different to those in the surrounding plasma. The electric field within the wing is lower than within the medium, which may be a reason for saturation of the projected electric potential in the polar cap. Chané *et al.* [2012] presented observational evidence of Alfvén wings at the Earth.

The formation of the Alfvén wings at the Earth's magnetosphere was studied by Ridley [2007] using MHD simulations. It was shown that the CPCP saturation occurs near the point when the solar wind becomes sub-Alfvénic. The analysis was later extended [Kivelson and Ridley, 2008] to define the CPCP using the solar wind and ionospheric properties. The idea behind such CPCP expression is that the impedance difference between the solar wind and the ionosphere causes a partial reflection of the Alfvén waves propagating into the ionosphere which limits the ionospheric potential. Thus, this reflection can be observed as a saturation of the E_y .

The Alfvén Mach number is also decisive as it controls how the bow shock compresses the solar wind plasma and magnetic field before they impinge on the Earth's magnetopause. Indeed, we found that the solar wind-magnetosphere coupling efficiency increases with increasing M_A . The effect of low solar wind M_A on the magnetosheath properties was extensively studied by Lavraud and Borovsky [2008] using global MHD simulations [see also Lavraud *et al.*, 2007, 2013]. These effects primarily arise from the fact that low M_A solar wind leads to low thermal beta (β) in the magnetosheath. In low β plasma the magnetic forces become dominant compared to the plasma pressure gradient. The magnetic tension and the magnetic pressure gradient forces cause particle acceleration perpendicular to the magnetic field along the flow streamlines. The acceleration enhances magnetosheath flows along the flanks of the magnetopause for south-north IMF orientations. Lavraud and Borovsky [2008] suggested that altered magnetosheath flows affect the CPCP saturation. During low M_A , the flow streamlines are more diverted around the magnetospheric obstacle. For a given E_y in the solar wind this enhanced diversion reduces the amount of magnetic flux available for the reconnection. This scenario was also studied and supported by the simulations done by Lopez *et al.* [2010]. The impact of magnetosheath flow properties to polar cap saturation have also been mentioned by Merkin *et al.* [2005].

Consistent with previous works [Ridley, 2005; Lavraud and Borovsky, 2008; Lopez *et al.*, 2010], our study shows a clear and in fact additional saturation of PCN for low M_A (< 3.3) conditions. The low M_A saturation can be explained by the altered magnetosheath flow pattern during low plasma beta as discussed above. Our results show that PCN saturates also during high M_A ($M_A > 7.3$) conditions (Figure 7 in particular), which indicates that the PCN saturation also has M_A -independent characteristics. In addition, as PCN increases almost linearly during intermediate M_A values ($3.3 < M_A < 7.3$, Figure 5), it is possible that the dominant mechanism causing the saturation is different for low and high M_A conditions. High M_A conditions arise, for example, when the solar wind density is high, and thus, such periods are related to a significant global compression in the size of the magnetosphere. This compression leads to the shortening of the X line, which could reduce CPCP (see also above discussion).

However, global MHD simulations by Lavraud and Borovsky [2008] suggest that the shortening of the X line cannot be the fundamental process in the CPCP saturation. On the contrary, Lavraud and Borovsky [2008] show that CPCP increases with increasing solar wind density (see their Figure 14). Thus, our observations raise the question whether the decreasing effect related to the X line length shortening becomes dominant over the density effect reported by Lavraud and Borovsky [2008] when M_A exceeds a certain threshold (about $M_A = 7.2$ according to our study).

Nine existing saturation models were compared against a global MHD simulation in the extensive study by Borovsky *et al.* [2009]. Simulation results did not support the models, which are based on the assumption that the saturation is caused by variations in the total amount of reconnection, like the X line length model. However, it should be noted that this simulation was done during moderate solar wind driving conditions ($v_{SW} = 300$ km/s, $B_z = -10$ nT, and $E_y = 3$ mV/m) and only for one M_A value of 1.9. Only the ionospheric Pedersen conductivity was varied in the simulations. In our study, the saturation during high M_A occurs when the E_y is above $E_y > 5$ mV/m.

Table 6. The Seasonal Occurrence of Sheath and Magnetic Cloud Events in Our Data Set

Season	Number of Events
Winter	12
Spring	22
Summer	17
Autumn	29

Our results have interesting implications for magnetic cloud and sheath-driven storms. These differences can be traced to different key solar wind conditions in these structures (see Figure 1). Sheaths have a clear tendency for high M_A conditions, while magnetic clouds are related to the lowest M_A values. As a consequence, sheaths typically have higher solar wind-magnetosphere coupling efficiencies than magnetic clouds. In addition, based on

the considerations discussed above, it seems that sheaths and magnetic clouds have a different dominant M_A -dependent CPCP saturation mechanism. For magnetic clouds the saturation may occur primarily due to the magnetosheath flow diversion (or other M_A -related mechanisms, while for sheaths the dominant cause may be the shortening of the X line length due to global magnetospheric compression.

The AE index also reveals interesting and unexpected features. When plotted against the solar wind driving E_Y , the index did not show any organization with M_A nor with any other investigated solar wind parameter. The reason why the AE index does not depend on M_A is not clear for the authors. While the PCN reacts rather rapidly to solar wind changes (see section 33.3), the AE responds in a more complicated manner. Auroral electrojets react to the changes in magnetospheric convection, similar to polar cap potential, but they also depend on the reconnection and substorm processes in the magnetotail. It is possible that the M_A dependence is masked by these processes. This idea is supported by the fact that if AE is plotted as a function of E_Y using the same time lag and window as for the PCN index (see Table 3), it shows M_A dependence (data not shown) but not as clearly as for the PCN . The auroral electrojets have seasonal variations [Guo *et al.*, 2014], which may also affect the results. Table 6 shows that our events occurred during all seasons, but there are significant differences, e.g., during the autumn there were 29 events, while during the winter only 12.

Lopez *et al.* [2009] studied the saturation of the ring current during high solar wind VB_S conditions. The ring current injection rate is typically estimated using the Burton formula [Burton *et al.*, 1975]

$$\alpha VB_S = \frac{Dst^*}{\tau} + \frac{\partial Dst^*}{\partial t}, \quad (7)$$

where α describes the geoeffectiveness, Dst^* is the pressure-corrected Dst , and τ is an empirically determined ring current decay time. The right-hand side of the equation is referred to as the ring current injection rate and it depends on VB_S . Because the polar cap potential saturates during high driving, as shown in this paper, it is expected that the ring current would saturate as well. However, this is not the case based on the simulations done by Lopez *et al.* [2009] and our results (See Figure S2 in supporting information). Lopez *et al.* [2009] suggested that during periods of strong B_S , the magnetosphere forms a quasi-steady reconnection region in the magnetotail which moves earthward and produces flux tubes that have plasma content lower than average, allowing them to enter the inner magnetosphere.

6. Conclusions

In this paper we have investigated the effect of key solar wind driving parameters on the solar wind-magnetosphere coupling efficiency and the saturation of the cross polar cap potential during sheath and magnetic cloud-driven magnetospheric storms. We also developed a method to define the most optimal time delay and window between the solar wind-magnetosphere coupling functions and the geomagnetic indices. The main conclusions of the present study are summarized as follows:

1. The PCN index shows a clear solar wind M_A dependence, while AE and $SYM-H$ do not.
2. PCN and AE indices saturate, but $SYM-H$ does not.
3. AE saturation is M_A independent, while PCN saturation depends clearly on M_A .
4. The coupling efficiency decreases with increasing solar wind driving electric field and increases with increasing M_A .

We report the first clear statistical evidence on polar cap potential saturation during high M_A conditions. This high M_A saturation occurred during intense solar wind driving. According to the authors' knowledge, none of the existing CPCP saturation models are able to describe the saturation during all M_A conditions. Thus, it is

possible that the mechanism for the saturation is different during low and high M_A regimens. CME sheaths and flux ropes have distinctly different M_A values and hence different coupling efficiencies. In addition, sheaths and magnetic clouds showed distinct differences in optimal time lags and window lengths. Turbulent sheath regions are more sensitive to the time shift and the averaging interval than smoother magnetic clouds.

The results presented in this study confirm that the solar wind-magnetosphere coupling efficiency depends strongly on the definition used. It is important to understand what different input functions and geomagnetic indices are describing and to what kind of assumptions they are based on. For example, despite the fact that both the PCN and AE are high-latitude indices, the former shows M_A dependence on the efficiency and the latter does not.

Acknowledgments

We acknowledge use of NASA/GSFC's Space Physics Data Facility's OMNIWeb and OMNI data. M. Myllys and E. Kilpua acknowledge Academy of Finland project 1267087 and M. Myllys also acknowledges the Finnish Academy of Science and Letters, Väisälä foundation for the financial support of the study.

References

- Akasofu, S.-I. (1981), Energy coupling between the solar wind and the magnetosphere, *Space Sci. Rev.*, *28*, 121–190.
- Bargatze, L. F., D. N. Baker, R. L. McPherron, and E. W. Hones Jr. (1985), Magnetospheric impulse response for many levels of geomagnetic activity, *J. Geophys. Res.*, *90*(A7), 6387–6394, doi:10.1029/JA090iA07p06387.
- Borovsky, J. E. (2008), The rudiments of a theory of solar wind/magnetosphere coupling derived from first principles, *J. Geophys. Res.*, *113*, A08228, doi:10.1029/2007JA012646.
- Borovsky, J. E., and H. O. Funsten (2003), Role of solar wind turbulence in the coupling of the solar wind to the Earth's magnetosphere, *J. Geophys. Res.*, *108*(A6), 1246, doi:10.1029/2002JA009601.
- Borovsky, J. E., B. Lavraud, and M. M. Kuznetsova (2009), Polar cap potential saturation, dayside reconnection, and changes to the magnetosphere, *J. Geophys. Res.*, *114*, A03224, doi:10.1029/2009JA014058.
- Burlaga, L. F. (1988), Magnetic clouds and force free fields with constant alpha, *J. Geophys. Res.*, *93*(A7), 7217–7224.
- Burton, R. K., R. L. McPherron, and C. T. Russell (1975), An empirical relationship between interplanetary conditions and Dst, *J. Geophys. Res.*, *80*(31), 4204–4214.
- Cassak, P. A., and M. A. Shay (2007), Scaling of asymmetric magnetic reconnection: General theory and collisional simulations, *Phys. Plasmas*, *14*(10), 102114.
- Chané, E., J. Saur, F. M. Neubauer, J. Raeder, and S. Poedts (2012), Observational evidence of Alfvén wings at the Earth, *J. Geophys. Res.*, *117*, A09217, doi:10.1029/2012JA017628.
- Clauer, C. R., R. L. McPherron, C. Searls, and M. G. Kivelson (1981), Solar wind control of auroral zone geomagnetic activity, *Geophys. Res. Lett.*, *8*(8), 915–918.
- Eriksson, S., R. E. Ergun, C. W. Carlson, and W. Peria (2000), The cross-polar potential drop and its correlation to the solar wind, *J. Geophys. Res.*, *105*(A8), 18,639–18,653, doi:10.1029/2000JA900033.
- Gonzalez, W. D., and E. Echer (2005), A study on the peak Dst and peak negative B_z relationship during intense geomagnetic storms, *Geophys. Res. Lett.*, *32*, L18103, doi:10.1029/2005GL023486.
- Guo, J., X. Feng, J. Zhang, P. Zuo, and C. Xiang (2010), Statistical properties and geoefficiency of interplanetary coronal mass ejections and their sheaths during intense geomagnetic storms, *J. Geophys. Res.*, *115*, A09107, doi:10.1029/2009JA015140.
- Guo, J., X. Feng, B. A. Emery, J. Zhang, C. Xiang, F. Shen, and W. Song (2011), Energy transfer during intense geomagnetic storms driven by interplanetary coronal mass ejections and their sheath regions, *J. Geophys. Res.*, *116*, A05106, doi:10.1029/2011JA016490.
- Guo, J., H. Liu, X. Feng, T. I. Pulkkinen, E. I. Tanskanen, C. Liu, D. Zhong, and Y. Wang (2014), MLT and seasonal dependence of auroral electrojets: IMAGE magnetometer network observations, *J. Geophys. Res. Space Physics*, *119*, 3179–3188, doi:10.1002/2014JA019843.
- Hairston, M. R., K. A. Drake, and R. Skoug (2005), Saturation of the ionospheric polar cap potential during the October–November 2003 superstorms, *J. Geophys. Res.*, *110*, A09S26, doi:10.1029/2004JA010864.
- Hill, T. W., A. J. Dessler, and R. A. Wolf (1976), Mercury and Mars: The role of ionospheric conductivity in the acceleration of magnetospheric particles, *Geophys. Res. Lett.*, *3*(8), 429–432.
- Huttunen, K. E. J., and H. E. J. Koskinen (2004), Importance of post-shock streams and sheath region as drivers of intense magnetospheric storms and high-latitude activity, *Ann. Geophys.*, *22*(5), 1729–1738.
- Huttunen, K. E. J., H. E. J. Koskinen, and R. Schwenn (2002), Variability of magnetospheric storms driven by different solar wind perturbations, *J. Geophys. Res.*, *107*(A7), 1121, doi:10.1029/2001JA900171.
- Huttunen, K. E. J., H. E. J. Koskinen, A. Karinen, and K. Mursula (2006), Asymmetric development of magnetospheric storms during magnetic clouds and sheath regions, *Geophys. Res. Lett.*, *33*, L06107, doi:10.1029/2005GL024894.
- Ilie, R., M. W. Liemohn, and A. Ridley (2010), The effect of smoothed solar wind inputs on global modeling results, *J. Geophys. Res.*, *115*, A01213, doi:10.1029/2009JA014443.
- Iyemori, T., and D. R. K. Rao (1996), Decay of the Dst field of geomagnetic disturbance after substorm onset and its implication to storm-substorm relation, *Ann. Geophys.*, *14*, 608–618, doi:10.1007/s00585-996-0608-3.
- Jing, H., J. Y. Lu, K. Kabin, J. S. Zhao, Z.-Q. Liu, Y. F. Yang, M. X. Zhao, and M. Wang (2014), MHD simulation of energy transfer across magnetopause during sudden changes of the IMF orientation, *Planet. Space Sci.*, *97*, 50–59.
- Kavosi, S., and J. Raeder (2015), Ubiquity of Kelvin-Helmholtz waves at Earth's magnetopause, *Nat. Commun.*, *6*, 7019.
- Kilpua, E. K. J., A. Isavnin, A. Vourlidis, H. E. J. Koskinen, and L. Rodriguez (2013a), On the relationship between interplanetary coronal mass ejections and magnetic clouds, *Ann. Geophys.*, *31*(7), 1251–1265.
- Kilpua, E. K. J., H. Hietala, H. E. K. Koskinen, D. Fontaine, and L. Turc (2013b), Magnetic field and dynamic pressure fluctuations in coronal mass ejection-driven sheath regions, *Ann. Geophys.*, *31*, 1559–1567.
- Kivelson, M. G., and A. J. Ridley (2008), Saturation of the polar cap potential: Inference from Alfvén wing arguments, *J. Geophys. Res.*, *113*, A05214, doi:10.1029/2007JA012302.
- Lavraud, B., and J. E. Borovsky (2008), Altered solar wind-magnetosphere interaction at low Mach numbers: Coronal mass ejections, *J. Geophys. Res.*, *113*, A00B08, doi:10.1029/2008JA013192.
- Lavraud, B., J. E. Borovsky, A. J. Ridley, E. W. Pogue, M. F. Thomsen, H. Reme, A. N. Fazakerley, and E. A. Lucek (2007), Strong bulk plasma acceleration in Earth's magnetosheath: A magnetic slingshot effect?, *Geophys. Res. Lett.*, *34*, L14102, doi:10.1029/2007GL030024.
- Lavraud, B., et al. (2013), Asymmetry of magnetosheath flows and magnetopause shape during low Alfvén Mach number solar wind, *J. Geophys. Res. Space Physics*, *118*, 1089–1100, doi:10.1002/jgra.50145.

- Lopez, R. E., J. G. Lyon, E. Mitchell, R. Bruntz, V. G. Merkin, S. Brogli, F. Toffoletto, and M. Wiltberger (2009), Why doesn't the ring current injection rate saturate?, *J. Geophys. Res.*, *114*, A02204, doi:10.1029/2008JA013141.
- Lopez, R. E., R. Bruntz, E. J. Mitchell, M. Wiltberger, J. G. Lyon, and V. G. Merkin (2010), Role of magnetosheath force balance in regulating the dayside reconnection potential, *J. Geophys. Res.*, *115*, A12216, doi:10.1029/2009JA014597.
- Lu, J. Y., H. Jing, Z. Q. Liu, K. Kabin, and Y. Jiang (2013), Energy transfer across the magnetopause for northward and southward interplanetary magnetic fields, *J. Geophys. Res. Space Physics*, *118*, 2021–2033, doi:10.1002/jgra.50093.
- Meng, C.-I. (1979), Polar cap variations and the interplanetary magnetic field, in *Dynamics of the Magnetosphere*, edited by S.-I. Akasofu, pp. 23–46, D. Reidel, Hingham, Mass.
- Merkin, V. G., A. S. Sharma, K. Papadopoulos, G. Milikh, J. Lyon, and C. Goodrich (2005), Global MHD simulations of the strongly driven magnetosphere: Modeling of the transpolar potential saturation, *J. Geophys. Res.*, *110*, A09203, doi:10.1029/2004JA010993.
- Neubauer, F. M. (1980), Nonlinear standing Alfvén wave current system at Io: Theory, *J. Geophys. Res.*, *85*(14), 1171–1178.
- Newell, P. T., T. Sotirelis, K. Liou, C. I. Meng, and F. J. Rich (2007), A nearly universal solar wind-magnetosphere coupling function inferred from 10 magnetospheric state variables, *J. Geophys. Res.*, *112*, A01206, doi:10.1029/2006JA012015.
- Nikolaeva, N. S., Y. I. Yermolaev, and I. G. Lodkina (2011), Dependence of geomagnetic activity during magnetic storms on the solar wind parameters for different types of streams, *Geomag. Aeron.*, *51*(1), 49–65.
- Palmroth, M., N. Partamies, J. Polvi, T. I. Pulkkinen, D. J. McComas, R. J. Barnes, P. Stauning, C. W. Smith, H. J. Singer, and R. Vainio (2007), Solar wind-magnetosphere coupling efficiency for solar wind pressure impulses, *Geophys. Res. Lett.*, *34*, L11101, doi:10.1029/2006GL029059.
- Pulkkinen, T. I., N. Partamies, K. E. J. Huttunen, G. D. Reeves, and H. E. J. Koskinen (2007), Differences in geomagnetic storms driven by magnetic clouds and ICME sheath regions, *Geophys. Res. Lett.*, *34*, L02105, doi:10.1029/2006GL027775.
- Pulkkinen, T. I., A. P. Dimmock, A. Osmane, and K. Nykyri (2015), Solar wind energy input to the magnetosheath and at the magnetopause, *Geophys. Res. Lett.*, *42*, 4723–4730, doi:10.1002/2015GL064226.
- Raeder, J., and G. Lu (2005), Polar cap potential saturation during large geomagnetic storms, *Adv. Space Res.*, *36*(10), 1804–1808.
- Reiff, P. H., and J. G. Luhmann (1986), Solar wind control of the polar-cap voltage, in *In Solar Wind Magnetosphere Coupling*, vol. 126, edited by Y. Kamide and J. A. Slavin, pp. 453–476, Terra Sci., Tokyo.
- Reiff, P. H., R. W. Spiro, and T. W. Hill (1981), Dependence of polar cap potential drop on interplanetary parameters, *J. Geophys. Res.*, *86*(A9), 7639–7648.
- Ridley, A. J. (2005), A new formulation for the ionospheric cross polar cap potential including saturation effects, *Ann. Geophys.*, *23*(11), 3533–3547.
- Ridley, A. J. (2007), Alfvén wings at Earth's magnetosphere under strong interplanetary magnetic fields, *Ann. Geophys.*, *25*(2), 533–542.
- Ridley, A. J., G. Lu, C. R. Clauer, and V. O. Papitashvili (1998), A statistical study of the ionospheric convection response to changing interplanetary magnetic field conditions using the assimilative mapping of ionospheric electrodynamics technique, *J. Geophys. Res.*, *103*(A3), 4023–4039, doi:10.1029/97JA03328.
- Rostoker, G. (1972), Geomagnetic indices, *Rev. Geophys.*, *10*(4), 935–950.
- Russell, C. T., G. Lu, and J. G. Luhmann (2000), Lessons from the ring current injection during the September 24, 25, 1998 storm, *Geophys. Res. Lett.*, *27*(9), 1371–1374.
- Russell, C. T., J. G. Luhmann, and G. Lu (2001), Nonlinear response of the polar ionosphere to large values of the interplanetary electric field, *J. Geophys. Res.*, *106*(A9), 18,495–18,504.
- Shepherd, S. G., R. A. Greenwald, and J. M. Ruohoniemi (2002), Cross polar cap potentials measured with Super Dual Auroral Radar Network during quasi-steady solar wind and interplanetary magnetic field conditions, *J. Geophys. Res.*, *107*(A7), 1094, doi:10.1029/2001JA000152.
- Stauning, P., and O. A. Troshichev (2008), Polar cap convection and PC index during sudden changes in solar wind dynamic pressure, *J. Geophys. Res.*, *113*, A08227, doi:10.1029/2007JA012783.
- Takalo, J., K. Mursula, and J. Timonen (2000), Role of the driver in the dynamics of a coupled-map model of the magnetotail: Does the magnetosphere act as a low-pass filter?, *J. Geophys. Res.*, *105*(A12), 27,665–27,672.
- Tanskanen, E., T. I. Pulkkinen, H. E. J. Koskinen, and J. A. Slavin (2002), Substorm energy budget during low and high solar activity: 1997 and 1999 compared, *J. Geophys. Res.*, *107*(A6), 1086, doi:10.1029/2001JA900153.
- Toth, G., et al. (2005), Space weather modeling framework: A new tool for the space science community, *J. Geophys. Res.*, *110*, A12226, doi:10.1029/2005JA011126.
- Troshichev, O. A., V. G. Andrezen, S. Vennerström, and E. Friis-Christensen (1988), Magnetic activity in the polar cap—A new index, *Planet. Space Sci.*, *36*(11), 1095–1102.
- Turner, N. E., W. D. Cramer, S. K. Earles, and B. A. Emery (2009), Geoefficiency and energy partitioning in CIR-driven and CME-driven storms, *J. Atmos. Sol. Terr. Phys.*, *71*(10), 1023–1031.
- Walsh, B. M., D. G. Sibeck, Y. Nishimura, and V. Angelopoulos (2013), Statistical analysis of the plasmaspheric plume at the magnetopause, *J. Geophys. Res. Space Physics*, *118*, 4844–4851, doi:10.1002/jgra.50458.
- Weimer, D. R., L. A. Reinleitner, J. R. Kan, L. Zhu, and S. I. Akasofu (1990), Saturation of the auroral electrojet current and the polar cap potential, *J. Geophys. Res.*, *95*(A11), 18,981–18,987.
- Wilder, F. D., C. R. Clauer, J. B. H. Baker, E. P. Cousins, and M. R. Hairston (2011), The nonlinear response of the polar cap potential under southward IMF: A statistical view, *J. Geophys. Res.*, *116*, A12229, doi:10.1029/2011JA016924.
- Yermolaev, Y. I., N. S. Nikolaeva, I. G. Lodkina, and M. Y. Yermolaev (2012), Geoeffectiveness and efficiency of CIR, sheath, and ICME in generation of magnetic storms, *J. Geophys. Res.*, *117*, A00L07, doi:10.1029/2011JA017139.
- Zurbuchen, T. H., and I. G. Richardson (2006), In-situ solar wind and magnetic field signatures of interplanetary coronal mass ejections, *Space Sci. Rev.*, *123*(1–3), 31–43.